ACS APPLIED NANO MATERIALS

www.acsanm.org

Article

Lighting Up WS_2 Nanoparticles on Ag Film via Plasmonic Enhancement and Exciton-Resonant Excitation

Yeshun Guo, Yuheng Mao, Jiancheng Xu, Tianxiang Yu, Mingcheng Panmai, Lidan Zhou, Shulei Li, Fu Deng,* and Sheng Lan*

Cite This: *ACS Appl. Nano Mater.* 2025, 8, 23665−23675

Read Online

ACCESS | Metrics & More | Article Recommendations | Supporting Information

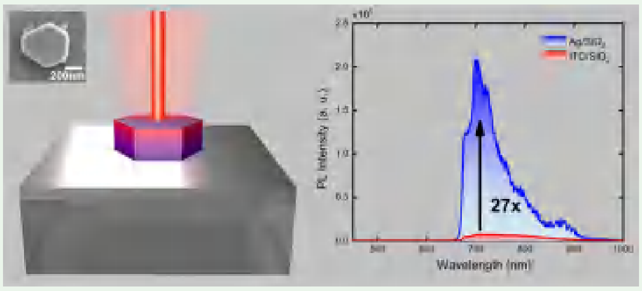

ABSTRACT: The manipulation of photoluminescence (PL) in two-dimensional (2D) materials presents a promising approach for the development of compact and tunable nanoscale light sources. Although monolayer transition metal dichalcogenides (TMDCs) exhibit strong excitonic emission owing to their direct bandgap, multilayer TMDCs generally experience reduced PL efficiency due to their indirect band structure. Here, we demonstrate that nanostructured WS_2 deposited on an Ag film exhibits markedly enhanced indirect PL emission, facilitated by metal film-assisted near-field enhancement and exciton-resonant excitation. Through systematic comparison of WS_2 nanoparticles on Ag and indium tin oxide (ITO) film under varying excitation wavelengths and powers, we show that the Ag substrate enhances PL intensity via metal film-induced field concentration, which is about 27 times stronger than that on the ITO film with the same excitation condition. Numerical simulations corroborate that the observed enhancement results from the enhancement effects of electric field localization and exciton-resonant absorption. Moreover, high-energy excitation induces additional PL peaks, which are attributed to hot carrier relaxation and direct transition phenomena. These findings provide fundamental insights into exciton dynamics within multilayer TMDC nanostructures and propose a scalable strategy for engineering their optical responses through hybrid platforms, thereby establishing a foundation for future applications in nonlinear optics, quantum photonics, and integrated 2D material-based optoelectronic devices.

KEYWORDS: *WS_2 nanoparticles, exciton, resonant excitation, plasmonic enhancement, photoluminescence*

■ INTRODUCTION

Two-dimensional (2D) TMDCs, such as MoS_2, WS_2, $MoSe_2$, and WSe_2, constitute a versatile class of atomically thin semiconductors characterized by exceptional and highly tunable optical and electronic properties.[1,2] Unlike their bulk counterparts, monolayer TMDCs exhibit a transition from an indirect to a direct bandgap within the visible spectral range, resulting in markedly enhanced light absorption and efficient radiative recombination at ambient temperature.[3,4] This direct bandgap, coupled with diminished dielectric screening and pronounced quantum confinement effects, leads to the formation of strongly bound excitons with binding energies exceeding 0.5 eV, which are substantially greater than those observed in conventional semiconductors.[5,6] The stability of these excitonic states facilitates the detailed investigation of quasiparticles, including neutral excitons, trions, and biexcitons. It enables phenomena such as spin-valley locking,[7] valley-selective circular dichroism,[8] and exciton-polariton formation.[9−11] Consequently, monolayer TMDCs have garnered significant interest for applications in valleytronics,[12] quantum photonics,[13] and ultrafast optoelectronics.[14] Furthermore, the ultrathin nature of TMDC monolayers permits their integration into nanophotonic platforms,[15−17] including dielectric metasurfaces,[18] photonic crystal slabs,[19] and plasmonic nanoparticles (NPs).[20] These hybrid systems can substantially enhance light-matter interaction strengths,[21,22] thereby advancing nonlinear optics,[23] all-optical modulation,[24] and electrically tunable light sources.[25] Nevertheless, critical challenges persist, notably the intrinsically low quantum yield of monolayers under ambient conditions, inefficient photon extraction, and the complexity associated with spatially precise tuning of excitonic interactions.[17] These limitations have prompted ongoing efforts to investigate alternative TMDC configurations and device architectures that aim to overcome current performance constraints.

On the other hand, although monolayer TMDCs have predominantly been the focus of research, multilayer and bulk

Received: September 30, 2025
Revised: November 19, 2025
Accepted: November 24, 2025
Published: December 2, 2025

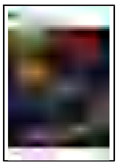

ACS Publications

https://doi.org/10.1021/acsanm.5c04516

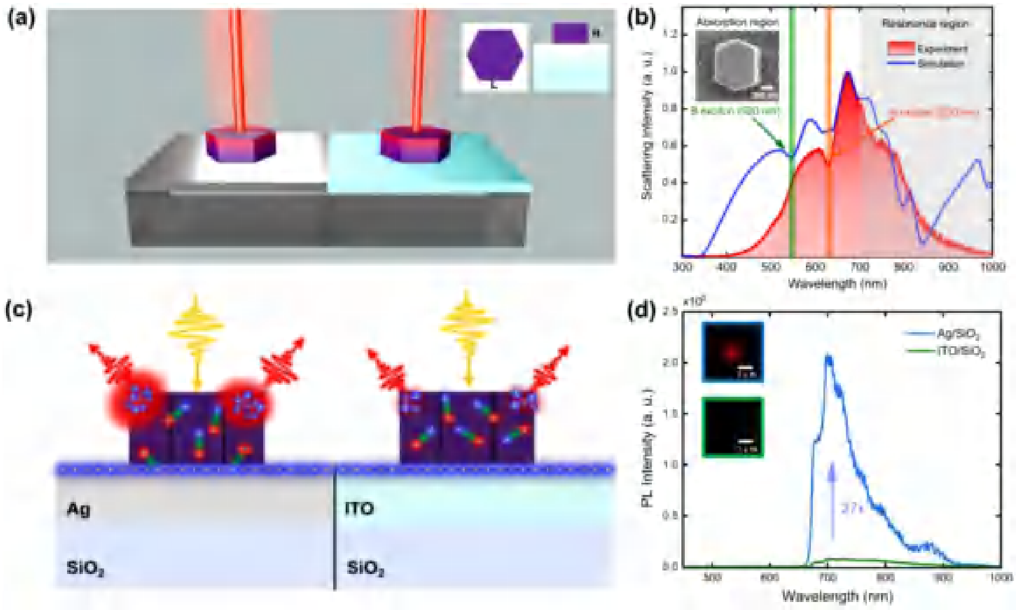

Figure 1. Conceptual illustration of PL enhancement in WS_2 NPs via exciton-resonant excitation. (a) Schematic of strong PL emission from a WS_2 NP placed on Ag/SiO_2 or ITO/SiO_2 substrates under femtosecond laser excitation. Insets show the top-view and cross-sectional view of the NP, with side length L and height H. (b) Experimental and simulated scattering spectra of a WS_2 NP on an Ag/SiO_2 substrate. The left inset shows the SEM image of the selected NP. The gray-shaded region distinguishes the resonance and absorption regimes. Pink and green vertical lines mark the resonance wavelengths of the A and B excitons, respectively. (c) Schematic of laser-induced carrier dynamics in WS_2 NPs on Ag/SiO_2 (left) and ITO/SiO_2 (right). Enhanced electron coupling at the Ag interface leads to stronger localized electron cloud formation and more efficient light emission compared to the ITO case. (d) PL spectra of WS_2 NPs on different substrates excited at the A exciton resonance (~630 nm) with the laser power of 3 mW. The left insets show the corresponding PL images captured by CCD.

TMDCs have recently attracted renewed attention due to their potential applications in scalable photonic and optoelectronic systems,[26] particularly when nanostructured.[27−29] While multilayer TMDCs possess an indirect bandgap that suppresses spontaneous emission in their unpatterned form, they present several significant advantages, including enhanced mechanical robustness, greater ease of fabrication, and compatibility with advanced nanofabrication techniques.[30] These multilayers can be etched or patterned into well-defined three-dimensional nanostructures,[31,32] such as disks,[33,34] pillars,[35] and gratings,[36,37] that support geometric optical modes,[38] including Mie resonances and quasi-bound states in the continuum (quasi-BICs).[39,40] Importantly, these modes can be spectrally tuned to coincide with the excitonic transitions that persist in multilayers, facilitating enhanced strong exciton-photon coupling.[41−43] Such interactions open new avenues for enhancing and controlling light absorption, emission, and nonlinear optical processes within the visible and near-infrared spectral regions.[30]

Recent investigations have demonstrated that patterned multilayer TMDC nanostructures exhibit enhanced second-harmonic generation (SHG) and other nonlinear optical phenomena through the resonant emission of exciton wavelengths, rendering them promising candidates for on-chip frequency conversion and ultracompact light sources.[44−48] Precisely engineered nanostructures can support exotic resonant modes, including Mie resonance,[38] anapole states,[49] quasi-BICs,[50] and edge-localized states,[51] which serve to confine and amplify optical fields. Nevertheless, the field enhancement attainable in pristine TMDC structures remains limited due to the large volume and weak intrinsic feedback mechanisms. This limitation can be addressed by integrating TMDCs with metallic substrates,[36] particularly highly reflective metallic films such as gold and silver in the visible spectrum,[39] which support surface plasmon resonances (SPRs) that substantially increase local field intensity and strengthen light-matter interactions.[43] Despite these advancements, the indirect band structure characteristic of multilayer TMDCs continues to constrain PL efficiency, presenting a fundamental challenge even in nanostructured and plasmonically enhanced configurations. PL enhancement in semiconductor nanostructures coupled with noble metal films has been extensively studied due to the strong local field confinement provided by plasmonic effects.[52] Previous studies have demonstrated PL enhancement in various semiconductor-metal hybrid systems, such as Si NPs on Au and Ag films, where near-field coupling enhances emission efficiency through an increased local density of optical states.[53,54] Similar enhancement mechanisms have been reported in TMDC monolayers integrated with metallic substrates or embedded in plasmonic nanocavities.[20,43] However, most of these works focus on direct-bandgap monolayers, while PL enhancement in indirect-bandgap bulk TMDCs remains underexplored.

In this study, we investigate the experimental realization of PL enhancement in WS_2 NPs integrated with an Ag film under varied optical excitation conditions. Our approach centers on resonant excitation at the A and B exciton energies and includes comparative analysis with transparent conductive ITO substrates. Through a combination of wavelength- and power-dependent PL spectroscopy and numerical simulations, we reveal that Ag substrates significantly amplify PL intensity via near-field enhancement and plasmon-assisted exciton generation. Numerical simulations confirm that this enhancement arises from both efficient carrier excitation and strong confinement of the optical field near the WS_2/Ag interface. Furthermore, we observe the emergence of secondary PL peaks

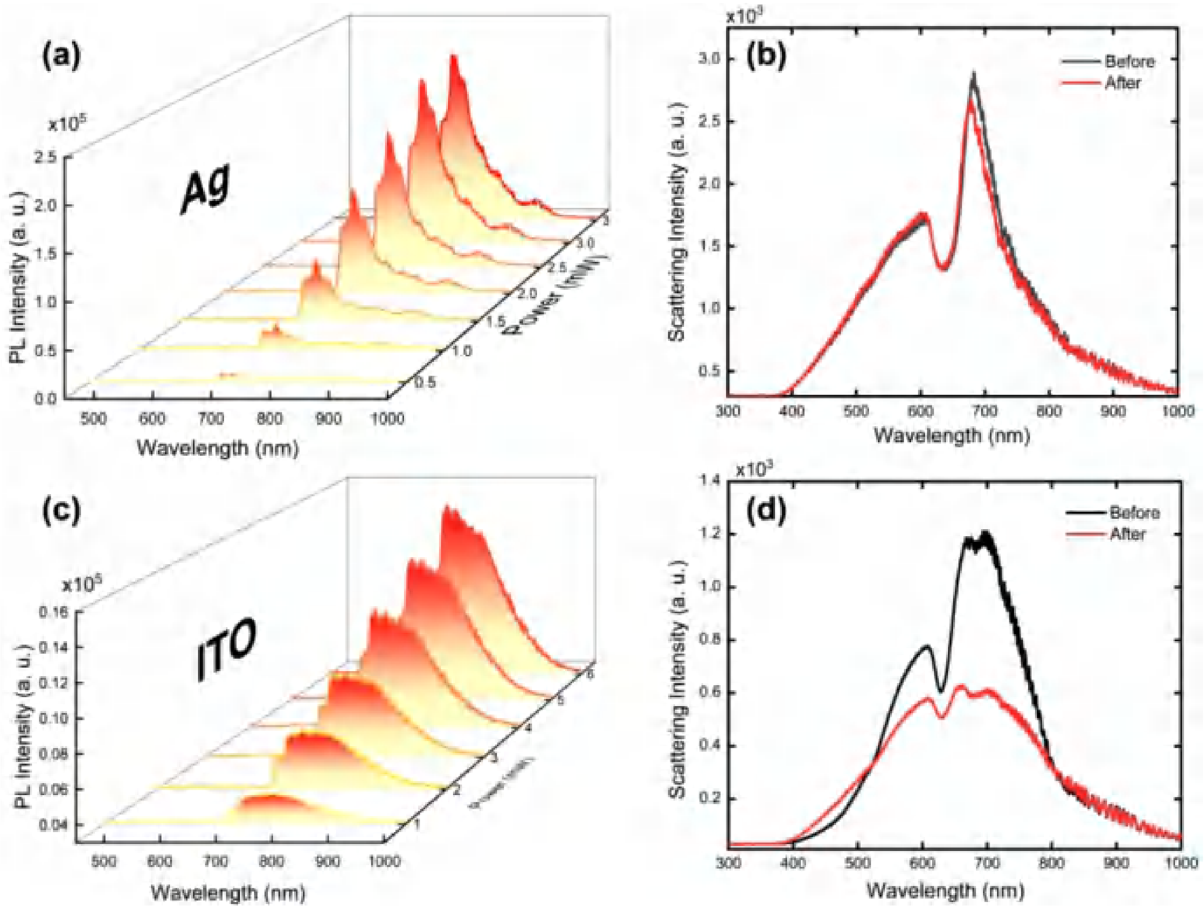

Figure 2. Evolution of PL spectra of WS_2 NPs on different substrates under exciton-resonant excitation. (a, c) Power-dependent PL spectra of WS_2 NPs on Ag/SiO_2 (a) and ITO/SiO_2 (c) substrates. (b, d) Scattering spectra of WS_2 NPs on Ag/SiO_2 (b) and ITO/SiO_2 (d) before and after laser excitation.

under high-energy excitation, revealing the influence of excitation wavelength on excitonic recombination pathways. Our results provide new insights into exciton-resonance-driven PL dynamics in nanostructured multilayer TMDCs and point toward practical strategies for developing high-efficiency, tunable light sources using hybrid TMDC-metallic platforms.

■ RESULTS AND DISCUSSION

Figure 1a presents a schematic illustration of a WS_2 NP placed on an Ag film, designed to enhance PL emission through exciton-resonant excitation. The NP exhibits a hexagonal geometry with a side length L and height H, as shown in the inset in the upper right corner. To explore the potential for PL enhancement, we investigated the dynamics of hot electrons in the hybrid structure under intense femtosecond laser excitation tuned to the A-exciton resonance wavelength. As depicted in Figure 1c, excitation promotes electrons in the exciton to higher energy states, forming a transient electron cloud. Meanwhile, holes are captured at the metal film surface,[55] facilitating efficient radiative recombination and, hence, enhanced PL emission. By contrast, ITO substrates, due to their lower free electron density in the visible range, do not support such hot electron dynamics. As a result, excitons tend to recombine without significant enhancement, resulting in much weaker PL signals due to a lower electron cloud density. The substrate of ITO film coated on SiO_2 was selected for comparison owing to its high electrical conductivity, which enables morphology characterization via scanning electron microscopy (SEM) without requiring additional conductive coatings. Furthermore, the refractive index of ITO closely matches that of SiO_2, rendering its impact on the optical scattering properties of WS_2 NPs negligible.[48]

To experimentally verify this PL enhancement mechanism, WS_2 NPs were fabricated and deposited onto Ag/SiO_2 substrates. The NPs were prepared using a simple procedure involving ultrasonic exfoliation and centrifugation of WS_2 powder to obtain a uniform suspension, as described in our previous work.[48] The resulting solution was to drop-cast onto well-grown and clean Ag/SiO_2 and ITO/SiO_2 substrates and allowed to dry naturally under ambient conditions. The structural and optical properties of the fabricated samples were characterized using SEM and dark-field microscopy, respectively. Figure 1b shows a representative SEM image, confirming the well-formed hexagonal geometry of the NPs. The scattering spectra obtained under dark-field illumination display two prominent peaks at ~690 nm and ~800 nm. The ~690 nm peak is attributed to the band-edge absorption, closely matching the absorption onset around 700 nm (see more examples in Figure S1 in Supporting Information). The resonance near 800 nm originates from the fundamental electric dipole Mie mode of the WS_2 NPs, which arises from displacement current oscillations within the high-index dielectric structure, as described in the previous works.[39,46] This mode may lead to enhanced scattering and field

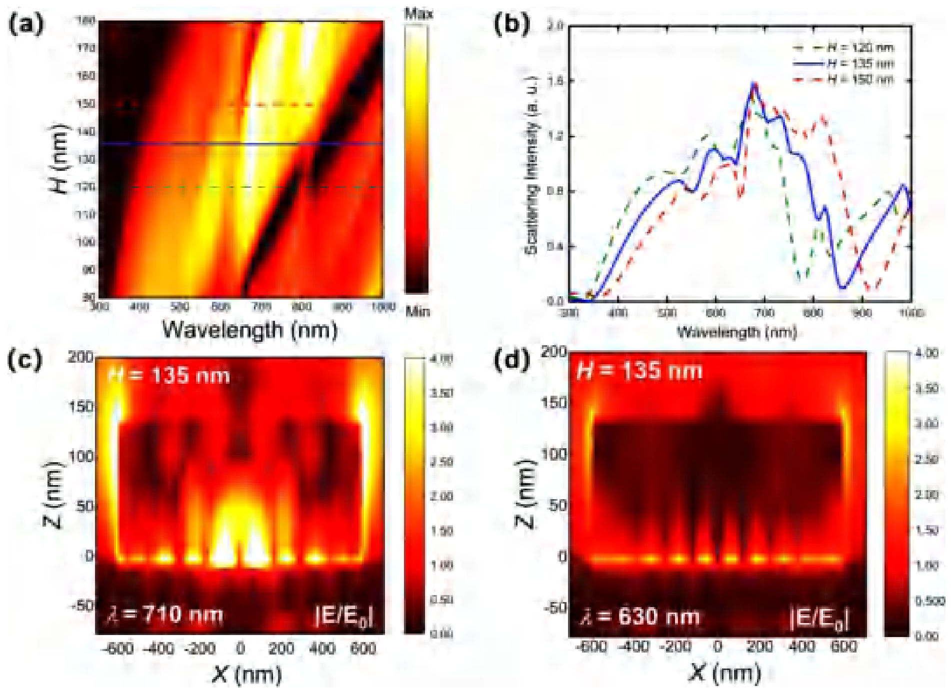

Figure 3. Numerical simulation of scattering and field distribution in WS_2 NPs on Ag/SiO_2. (a) Simulated scattering spectra as a function of WS_2 thickness for a fixed NP diameter ($L = 1$ μm). (b) Selected scattering spectra for representative thicknesses extracted from horizontal cuts in (a), matching experimental conditions. Electric field distributions at emission (c) and excitation (d) wavelengths for a NP with height $H = 135$ nm, showing strong field confinement in the gap between the NP and Ag substrate.

confinement characteristic of TMDC-based dielectric nanoresonators. A distinct dip around 630 nm, marked by a red vertical line, corresponds to the A exciton of bulk WS_2, while the B exciton (~520 nm) appears as a shoulder in the spectrum.

To further understand the optical behavior of the hybrid cavity, we performed numerical simulations using the finite-difference time-domain (FDTD) method. The simulated scattering spectrum, also shown in Figure 1b, is in agreement with the experimental results. Notably, the B exciton feature is more pronounced in the simulation, and several optical resonances emerge in the longer-wavelength region that are absent in the experimental data. These discrepancies may arise from the limited resolution of the spectrometer beyond 850 nm and potential deviations between the refractive index of WS_2 used in simulations (sourced from literature[56]) and the actual optical constants of our samples. Nonetheless, the simulation successfully reproduces the major spectral features, validating its utility in explaining the resonance behavior of the system.

Building on the observed scattering characteristics, we probed the PL response by exciting the WS_2 NPs with a femtosecond laser generated via an OPO with the wavelength tuned to ~630 nm, resonant with the A exciton. As illustrated in Figure 1d, WS_2 NPs on Ag/SiO_2 exhibit strong broadband PL emission extending beyond the excitation wavelength. The broadband PL emission extending beyond the excitation wavelength arises from hot-electron-induced luminescence involving both direct and phonon-assisted indirect transitions in WS_2. Under intense femtosecond excitation, energetic carriers relax through multiple pathways before radiative recombination, resulting in a broad emission spectrum. Such behavior is analogous to broadband or white-light emission reported in dielectric-metal hybrid systems, including Au and Si nanostructures.[53,54] For comparison, analogous measurements were carried out on WS_2 NPs deposited on ITO/SiO_2 substrate under identical excitation conditions. It is noted that the application of a metallic film can enhance the reflection of signals from the sample, thereby increasing the collection efficiency, as evidenced by the enhancement of the PL signal. Quantitatively, the PL intensity from the WS_2 NP on Ag/SiO_2 was approximately 27 times greater than that on ITO/SiO_2. This significant enhancement is attributed to the amplification of the local electromagnetic field, which facilitates efficient exciton generation and radiative recombination. It is noted that the PL emission from WS_2 NP on Ag film is dominated by the hot-electron luminescence,[53,54] which is different from the PL emission of direct band transition in their monolayer form,[10] causing the broadband PL emission, similar to the case of traditional semiconductor Si nanostructure. These results clearly demonstrate the advantage of Ag substrates in enhancing PL emission from WS_2 NPs under resonant excitation conditions. A more detailed analysis of this enhancement mechanism is presented in the following sections.

To further elucidate the pronounced PL enhancement observed in WS_2 NPs on Ag film substrates, we examine the evolution of PL spectra under A exciton excitation across different substrates, as shown in Figure 2. Figure 2a,c presents the power-dependent PL spectra of WS_2 NPs deposited on Ag/SiO_2 and ITO/SiO_2 substrates, respectively. In both cases, the PL intensity increases with excitation power. However, a key difference lies in the spectral characteristics: WS_2 NPs on Ag/SiO_2 consistently exhibit a sharp and prominent emission peak near 700 nm, while those on ITO/SiO_2 show broader and less-defined spectra. This contrast arises from differences in their linear optical properties, as illustrated in Figure 2b,d. Specifically, the scattering spectrum of the WS_2−Ag hybrid

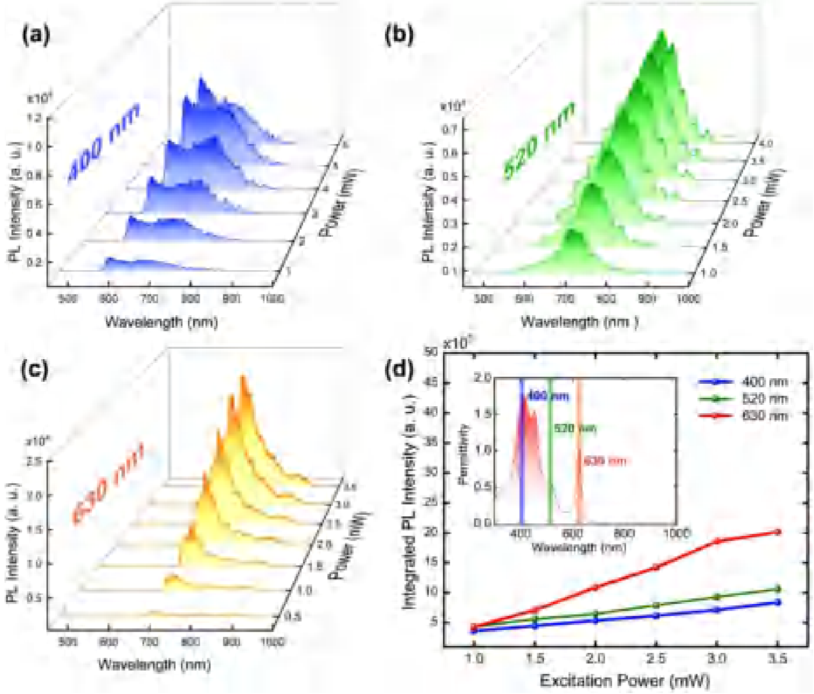

Figure 4. PL emission behavior of WS_2 NPs on Ag/SiO_2 under different excitation wavelengths. (a−c) Power-dependent PL spectra under excitation at 400 nm (a), 520 nm (b), and 630 nm (c), respectively. (d) Integrated PL intensity as a function of excitation power for the three wavelengths. The inset shows the imaginary part of the refractive index of multilayer WS_2, with vertical lines indicating the excitation wavelengths.

system (Figure 2b) reveals a pronounced peak near 700 nm. The emission feature centered near 700 nm originates from an indirect transition involving phonon-assisted photon emission in bulk/multilayer WS_2. In this process, electron recombination occurs between the valence-band maximum and the conduction-band minimum, with phonons providing the necessary momentum to satisfy conservation rules.[35] This phonon-assisted recombination pathway is characteristic of indirect-bandgap TMDCs and has been observed in multilayer WS_2 and related materials.[57] In contrast, WS_2 NPs on ITO (Figure 2d) initially display a well-defined scattering peak near 700 nm, but the intensity diminishes following PL measurements, likely due to laser-induced annealing or thermal modification of the ITO surface. These substrate-dependent changes in the scattering behavior suggest that PL emission is mediated through different optical channels, thereby giving rise to the observed variations in spectral shape. Notably, in the Ag-supported sample, a weak additional peak near 900 nm is also detected. The weak resonance feature observed near 900 nm in the Ag-supported WS_2 sample arises from the hybridization between the dielectric Mie-type mode of the WS_2 NPs and the mirror-induced image mode in the Ag film. This coupling forms a hybrid photonic-plasmonic resonance at longer wavelengths than the fundamental Mie resonance, leading to weak but detectable PL emission in the near-infrared range. Similar hybrid resonances have been reported in WS_2 and other high-index nanostructures coupled with metallic substrates.[39] However, due to the limited spectrometer resolution in the near-infrared range, our subsequent analysis focuses primarily on the dominant emission feature around 700 nm.

To gain deeper insight into the origin of the enhanced PL emission, we conducted numerical simulations of the linear optical response of the WS_2−Ag hybrid system using the FDTD method, as shown in Figure 3. Figure 3a presents simulated scattering spectra for WS_2 NPs of varying thicknesses placed on Ag film. The thickness was tuned to aligning with experimental observations, taking into account minor variations among fabricated samples. The in-plane dimensions were derived from SEM images (refer to Figure 1b). The simulations reveal strong scattering peaks above 650 nm, which redshift progressively with increasing WS_2 thickness. For thicknesses exceeding 150 nm, additional peaks emerge due to the excitation of higher-order optical modes. A characteristic dip at longer wavelengths is also observed, which redshifts with increasing thickness; this feature is attributed to an anapole state, resulting from destructive interference between electric dipole and toroidal dipole moments.[33] To enable direct comparison with the experimental results, Figure 3b presents the simulated scattering spectra for WS_2 thicknesses approximately 135 nm, corresponding to the samples employed in PL measurements. This thickness range, spanning from 130 to 140 nm, is corroborated by WS_2 power measurements (see Figure S2 in Supporting Information for further details). Minor discrepancies in spectral features may result from idealized geometries assumed in simulation, particularly the shape of the NP, which could be further refined in future studies. To visualize the spatial distribution of the optical field enhancement within the hybrid structure, Figure 3c,d display the simulated electric field intensities at both the excitation and emission wavelengths. A significant field enhancement is observed in the gap region between the WS_2 NP and the Ag film. At the emission wavelength (~710 nm), the local field intensity exceeds the incident field by more than a factor of 8, indicating strong confinement of optical energy. This substantial enhancement of the near-field intensity provides the physical basis for the dramatically increased PL emission observed in Figures 1 and 2, confirming the critical role of the hybrid dielectric-metal nanocavity formed by the dielectric NP and the underlying Ag

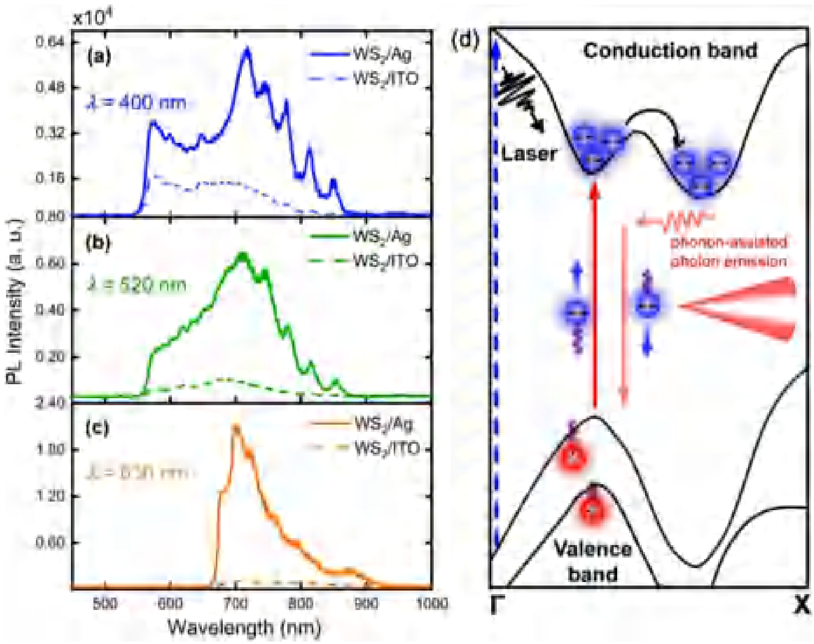

Figure 5. Comparison of PL emission from WS_2 NPs on Ag and ITO substrates and corresponding band structure analysis. (a−c) PL spectra of WS_2 NPs on Ag/SiO_2 under excitation at different wavelengths (5 mW). Corresponding spectra for WS_2 on ITO/SiO_2 are shown as dashed lines for comparison. The weak fringes at long wavelength part are artifacts resulting from the dichroic mirror and are not related to the intrinsic optical response of the WS_2 NPs. (d) Schematic band diagram of WS_2 illustrating electronic transitions under excitation at different wavelengths. Blue-dashed, red-solid and orange-solid arrows represent various excitation channels, while the indirect transition is realized via phonon-assisted photon emission in bulk WS_2.

film. The near-field enhancement observed in the WS_2−Ag hybrid structure originates from the coupling between the localized Mie-type optical mode of the WS_2 NP and its mirror-induced field in the Ag film, forming a hybrid dielectric-metal nanocavity.[39] This configuration differs from a conventional plasmonic gap cavity, as it combines dielectric confinement with mirror-enhanced field localization, leading to efficient emission enhancement.[20] Similar hybrid effects have been reported in dielectric nanoparticle-on-mirror systems supporting hybrid Mie-plasmon modes.[58] In addition, the electric field of WS_2 of NPs on the Ag film is stronger than that on the ITO film, consistent with the realization of PL enhancement (see Figure S3 in Supporting Information for more details). It should be noted that the simulated near-field enhancement within the hybrid WS_2 on Ag film system exceeds 8-fold at the emission wavelength, serving as the primary driver of the observed 27 times PL enhancement. However, the PL intensity does not scale linearly with the field enhancement, as it is also influenced by the Purcell effect, absorption enhancement, and radiation efficiency.[58] The strong field confinement at the WS_2 NP and metal interface accelerates spontaneous emission, increases exciton generation efficiency, and improves photon outcoupling through nanoantenna-assisted radiation channels, collectively accounting for the pronounced PL enhancement under exciton-resonant excitation.

Building upon the observed PL enhancement in WS_2 NPs coupled to Ag film under A exciton-resonant excitation, we further investigate the wavelength dependence of PL by varying the excitation wavelength. Figure 4 presents the PL emission behavior of a WS_2 NP on an Ag/SiO_2 substrate under excitation at 400, 520, and 630 nm, corresponding to the interband transition, the B exciton, and the A exciton of bulk WS_2, respectively, as indicated by the imaginary part of the refractive index shown in the inset of Figure 4d. Under 400 nm excitation, the incident photons drive interband carrier transitions, leading to electron−hole recombination and broadband PL emission, as shown in Figure 4a. In contrast, when the excitation wavelength is tuned to 520 or 630 nm, close to the B and A exciton resonances, PL spectra exhibit narrower peaks centered around ∼700 nm (Figure 4b,c). Notably, the PL intensity is substantially higher under 630 nm excitation compared to 520 nm, as confirmed by the spectral data.

To quantitatively compare PL responses across these excitation wavelengths, the integrated PL intensities are plotted in Figure 4d as a function of laser power. All three excitation regimes exhibit a linear increase in PL with increasing power; however, the PL intensity under 630 nm excitation is significantly stronger than that observed at 520 or 400 nm. This enhancement at the A-exciton resonance is attributed to its strong optical absorption and narrow spectral line width, which together facilitate a more efficient photon-to-exciton transition. As illustrated in the inset of Figure 4d, the A exciton resonance coincides with a peak in the imaginary part of the refractive index, confirming optimal energy absorption at this wavelength.[56] Although 520 nm excitation lies near the B exciton resonance, its relatively weaker oscillator strength leads to less efficient coupling and hence lower PL intensity. Still, PL under 520 nm excitation is stronger than that under 400 nm excitation. Despite the highest absorption of WS_2 occurring near 400 nm, PL emission at this wavelength is relatively weak. This is likely due to significant nonradiative losses: a considerable portion of the absorbed energy at 400 nm is converted into heat through electron−phonon interactions rather than being radiatively recombined, thereby suppressing PL emission. These results underscore the importance of exciton-resonant excitation, particularly at the A exciton wavelength, for maximizing PL efficiency in WS_2 NPs coupled to metallic substrates. It is noted that although the PL signal excited at 630 nm is significantly stronger than those excited at 400 and 520 nm, the PL image captured by the CCD closely resembles that obtained at 520 nm. This discrepancy is attributed to the influence of the filters used in our experiment, which impede the accurate capture of the true CCD image (see Figure S4 in Supporting Information). This limitation can be addressed in future studies by employing more suitable filters.

Expanding upon our investigation of PL enhancement under exciton-resonant excitation, Figure 5 provides a comprehensive analysis of the substrate-dependent PL behavior of WS_2 NPs. Figure 5a−c compares the PL spectra of WS_2 NPs deposited on Ag and ITO substrates under excitation at 400, 520, and 630 nm, using a fixed laser power of ∼5 mW for all measurements. In every excitation scenario, the PL intensity from WS_2 NPs on Ag film is significantly stronger than that from those on ITO substrates. This enhancement is attributed to the localized electric field amplification induced by dielectric-metal hybrid nanocavity. Such enhancement effects in dielectric-metal structures are well established as mechanisms for boosting both linear and nonlinear optical responses in nanoscale systems.[32,36] Across all excitation conditions, a dominant emission peak appears near 710 nm, which aligns well with the electronic band structure of bulk WS_2, as illustrated in Figure 5d. Under exciton-resonant excitation at 630 nm (A exciton) and 520 nm (B exciton), photoexcited carriers are promoted directly into specific valleys in the conduction band, as indicated by the blue and orange dashed arrows in Figure 5d. These carriers then undergo intervalley relaxation to the lowest conduction band minimum, where they recombine with holes in the valence band, yielding PL emission near 710 nm, corresponding to the indirect bandgap of bulk WS_2 (∼1.7 eV).[59]

By contrast, excitation at 400 nm injects free carriers into the conduction band at much higher energies. Most of these carriers relax to the lowest-energy valley and recombine to emit photons at ∼710 nm, similar to exciton-resonant excitation. However, a fraction of the high-energy carriers can recombine with holes in higher-energy valence band valleys, giving rise to PL emission at photon energies greater than 1.7 eV. This process results in a secondary spectral peak at shorter wavelengths, clearly observed in the 400 nm excitation data shown in the upper panel of Figure 5a. These results collectively clarify the underlying mechanisms governing PL emission in WS_2 NPs. The significantly stronger PL emission observed on Ag substrates, particularly under A exciton excitation, is a direct consequence of enhanced near-field coupling facilitated by electric field enhancement effects. Specifically, Ag film substrates enable an order-of-magnitude increase in PL intensity at 630 nm, underscoring the importance of resonant excitation conditions in maximizing emission efficiency. To elucidate the significance of resonant excitation in the PL enhancement of mirror-coupled WS_2 NPs, wavelength-dependent excitation using a femtosecond laser in the range of 615−640 nm was conducted. As shown in Figure S5 in the Supporting Information, the results confirm that the strongest PL signal occurs at an excitation wavelength of 630 nm. Additionally, it should be noted that the fringes observed in Figure 5a−c are artifacts resulting from the dichroic mirror (see Figure S6 in the Supporting Information). These artifacts do not impact the principal conclusions of our study. In addition, the reproducibility of the PL enhancement was verified by repeated measurements on several WS_2 NPs under identical excitation conditions, all exhibiting consistent enhancement behavior. As the enhancement primarily originates from exciton-resonant excitation rather than geometric variation, it is only weakly dependent on NP size. Owing to the random size distribution of chemically derived WS_2 NPs, large-scale statistical analysis was not feasible; nevertheless, the reproducible results across multiple measurements confirm the reliability of the observed enhancement effect.

The observed PL enhancement in WS_2 NP on Ag films is consistent with previously reported plasmonic enhancement effects in semiconductor-metal hybrid systems, such as Si NPs coupled with noble metal films.[53] However, unlike those systems, the enhancement in WS_2 originates from exciton-resonant excitation in an indirect-bandgap regime, where near-field confinement and excitonic transitions cooperatively enhance PL emission. Beyond providing insights into the carrier dynamics and band structure of bulk WS_2, these findings highlight the potential of plasmon-enhanced nanostructures as platforms for exploring nonlinear optical phenomena in TMDCs. While the present study employed a simple fabrication approach to realize PL enhancement, the observed electric field amplification remains limited by the structural simplicity of the system. Future performance could be further improved by engineering nanocavities to support advanced photonic states, such as anapole modes,[49] bound states in the continuum (BIC),[41] and guided-mode resonances.[57] Such enhancements are feasible through integration of TMDC nanostructures with advanced and high-resolution fabrication techniques, including electron beam lithography (EBL) and reactive ion etching (RIE).[32] It is worth emphasizing that, unlike the widely studied monolayer TMDC-metal hybrid systems, where direct exciton−plasmon coupling dominates the enhancement mechanism,[9,20] our study explores a distinct physical regime based on multilayer WS_2 nanostructures integrated with an Ag film. In this indirect-bandgap system, PL enhancement arises primarily from exciton-resonant excitation and near-field amplification within a hybrid dielectric-metal nanocavity, rather than from coherent plasmon-exciton hybridization. This distinction highlights a complementary mechanism for achieving strong light emission in materials traditionally limited by indirect recombination.[35] The demonstrated WS_2−Ag configuration thus provides a promising platform for advancing hybrid 2D nanophotonics, offering potential applications in bright nanoscale light sources, surface-enhanced sensors, and nonlinear optical devices.[30] These findings extend the scope of plasmon-assisted photonic research beyond monolayer TMDCs and open a new direction for exploiting multilayer or bulk 2D materials in active optoelectronic and quantum photonic technologies.

■ CONCLUSIONS

In summary, we have demonstrated a significant enhancement of PL emission in WS_2 NPs by leveraging exciton-resonant excitation and electric field enhancement in the hybrid dielectric-metal nanocavity. Systematic comparisons across different substrates reveal that the Ag film provides more than an order-of-magnitude increase in PL intensity relative to ITO counterparts. This enhancement is enabled by near-field enhancement and efficient photon transition at the A exciton resonance. Wavelength-dependent excitations show that PL emission is highly selective, peaking near 710 nm under 630 nm excitation, which corresponds to the A-exciton excitation of bulk WS_2. Numerical simulations corroborate the experimental results, indicating that the metallic substrate supports enhanced optical confinement in the gap region, leading to increased excitation and emission efficiency. Furthermore, excitation at higher photon energies (e.g., 400 nm) induces broadband emission, with secondary peaks arising from higher-energy carrier recombination pathways, consistent with the electronic band structure of bulk WS_2. Our findings provide clear insight into metallic substrate-mediated PL modulation in multilayer TMDC nanostructures and underscore the critical role of exciton resonance and electric-field enhancement in tailoring emission behavior. Beyond elucidating the origin of PL enhancement, this work offers a robust platform for engineering nonlinear and quantum optical responses in TMDC-based photonic devices.

■ METHODS

Sample Preparation and Characterization. WS_2 NPs used in our work were synthesized from WS_2 powder purchased from Sixcarbon Tech, Shenzhen. The synthesis procedure was as follows: approximately 12 mg of the powder was measured and placed at the bottom of a test tube, to which 3 mL of deionized water was added for dilution. The test tube was then placed in an ultrasonic cleaner and sonicated for 10 min to ensure uniform dispersion of the WS_2 powder. After sonication, 1 mL of the upper suspension was extracted and transferred to a new test tube, where additional deionized water was added to bring the total volume to 3 mL for further dilution. To maintain a low temperature during sonication and prevent agglomeration that could compromise sample quality, ice cubes were added to the ultrasonic cleaner. The WS_2 suspension in the new test tube underwent a second sonication for an additional 10 min. Subsequently, the test tube was centrifuged at 6000 rpm to facilitate processing of the WS_2. This cycle of sonication and centrifugation was repeated three times to ensure complete dispersion of the WS_2 powder in deionized water. Finally, the middle layer of the suspension was carefully extracted and allowed air-dry naturally on various substrates, completing the sample preparation. The morphology of the resulting WS_2 NPs was characterized using scanning electron microscopy (SEM; Zeiss).

Optical Characterization. The optical properties of the hybrid WS_2 NP situated on the Ag/SiO_2 substrate were measured using an inverted microscope (Observer A1, Zeiss) equipped with both white light and femtosecond laser excitation sources. Visible laser pulses from an optical parametric oscillator (OPO-X, Coherent), pumped by an 800 nm femtosecond laser (Mira 900S, Coherent; pulse duration of 130 fs and repetition rate of 76 MHz), were employed to excite the WS_2 NP on the metal film structure. Additionally, the 400 nm laser pulse was generated through second-harmonic generation of the fundamental 800 nm pulse. The excitation was focused through a 100× objective lens, with polarization controlled by a custom-built polarizer. The resulting PL emissions from the WS_2 NP were collected through the same objective lens and directed either to a spectrometer (SR-500i-B1, Andor) for spectral analysis or to charge-coupled device cameras (DU970N, Andor) for imaging. In all measurements, the excitation light was linearly polarized, and its polarization direction was kept fixed to ensure consistency and minimize polarization-dependent variations in excitation efficiency. For experiments using different excitation wavelengths generated from separate laser sources, the polarization orientations were carefully aligned to maintain the same direction. The WS_2 NP samples were also kept stationary during measurements to ensure reproducibility under identical polarization conditions.

Numerical Simulation. The scattering spectra and enhancement of the electric field in a WS_2 NP positioned on an Ag/SiO_2 film structure were modeled using the finite-difference time-domain (FDTD) method, specifically employing Lumerical FDTD Solutions software. In this simulation, the WS_2 NP was represented as a regular hexagonal prism with a thickness of 135 nm and a side length of 600 nm, parameters that were adjusted based on experimental measurements obtained from SEM images. The refractive index values of WS_2 were adopted from the relevant literature.[56] The thickness of the Ag film was established at 50 nm, with its dielectric constants referenced from the literature.[60] A self-adaptive mesh was employed throughout the entire structure to ensure high precision, and perfectly matched layer (PML) conditions were implemented in all directions to effectively confine the simulation domain. The minimum mesh size was set to 1 nm for both the WS_2 NP and the Ag film area.

■ ASSOCIATED CONTENT

Supporting Information

The Supporting Information is available free of charge at https://pubs.acs.org/doi/10.1021/acsanm.5c04516.

> Scattering spectra of more WS_2 nanoparticles; SEM characterization of the thickness of WS_2 nanoparticles; electric field distributions of WS_2 nanoparticles; CCD images with different filters; excited wavelength-dependent PL intensity; spectral artifact caused by the dichroic mirror (PDF)

■ AUTHOR INFORMATION

Corresponding Authors

Fu Deng − *Guangdong Provincial Key Laboratory of Nanophotonic Functional Materials and Devices, School of Optoelectronic Science and Engineering, South China Normal University, Guangzhou 510006, China;* orcid.org/0009-0004-8147-1812; Email: dengfu@m.scnu.edu.cn

Sheng Lan − *Guangdong Provincial Key Laboratory of Nanophotonic Functional Materials and Devices, School of Optoelectronic Science and Engineering, South China Normal University, Guangzhou 510006, China;* orcid.org/0000-0002-7277-0042; Email: slan@scnu.edu.cn

Authors

Yeshun Guo − *Guangdong Provincial Key Laboratory of Nanophotonic Functional Materials and Devices, School of Optoelectronic Science and Engineering, South China Normal University, Guangzhou 510006, China*

Yuheng Mao − *Guangdong Provincial Key Laboratory of Nanophotonic Functional Materials and Devices, School of Optoelectronic Science and Engineering, South China Normal University, Guangzhou 510006, China;* orcid.org/0009-0007-6267-7120

Jiancheng Xu − *Guangdong Provincial Key Laboratory of Nanophotonic Functional Materials and Devices, School of Optoelectronic Science and Engineering, South China Normal University, Guangzhou 510006, China*

Tianxiang Yu − *State Key Laboratory of Optoelectronic Materials and Technologies and School of Electronics and Information Technology, Sun Yat-Sen University, Guangzhou 510275, China*

Mingcheng Panmai − *School of Physical and Mathematical Sciences, Nanyang Technological University, Singapore 637371, Singapore;* orcid.org/0009-0003-0291-6805

Lidan Zhou − *State Key Laboratory of Optoelectronic Materials and Technologies and School of Electronics and Information Technology, Sun Yat-Sen University, Guangzhou 510275, China;* orcid.org/0000-0003-3146-9082

Shulei Li − *School of Optoelectronic Engineering, Guangdong Polytechnic Normal University, Guangzhou 510665, China*

Complete contact information is available at: https://pubs.acs.org/10.1021/acsanm.5c04516

Author Contributions

Y.G., T.Y., and L.Z. fabricated the samples; Y.G., T.Y., Y.M., and M.P. carried out the optical measurements; Y.G. and S.-L.L. carried out the numerical simulations; Y.G., F.D., and S.L. analyzed the data and wrote the manuscript; S.L. and F.D. supervised the project. All the authors read and commented on the manuscript.

Funding

S. Lan acknowledges support from the National Natural Science Foundation of China (Grant Nos. 12174123 and 12374347). L. Zhou acknowledges support from the National Natural Science Foundation of China (Grant No. 92365112). S. Li acknowledges support from the Guangdong Basic and Applied Basic Research Foundation (Grant No. 2025A1515012291).

Notes

The authors declare no competing financial interest.

■ REFERENCES

(1) Manzeli, S.; Ovchinnikov, D.; Pasquier, D.; Yazyev, O. V.; Kis, A. 2D transition metal dichalcogenides. *Nat. Rev. Mater.* **2017**, *2* (8), 17033.

(2) De Abajo, F. J. G.; Basov, D. N.; Koppens, F. H. L.; Orsini, L.; Ceccanti, M.; Castilla, S.; Cavicchi, L.; Polini, M.; Gonçalves, P. A. D.; Costa, A. T.; Peres, N. M. R.; Mortensen, N. A.; Bharadwaj, S.; Jacob, Z.; Schuck, P. J.; Pasupathy, A. N.; Delor, M.; Liu, M. K.; Mugarza, A.; Merino, P.; Cuxart, M. G.; Chávez-Angel, E.; Švec, M.; Tizei, L. H. G.; Dirnberger, F.; Deng, H.; Schneider, C.; Menon, V.; Deilmann, T.; Chernikov, A.; Thygesen, K. S.; Abate, Y.; Terrones, M.; Sangwan, V. K.; Hersam, M. C.; Yu, L.; Chen, X.; Heinz, T. F.; Murthy, P.; Kroner, M.; Smolenski, T.; Thureja, D.; Chervy, T.; Genco, A.; Trovatello, C.; Cerullo, G.; Dal Conte, S.; Timmer, D.; De Sio, A.; Lienau, C.; Shang, N.; Hong, H.; Liu, K.; Sun, Z.; Rozema, L. A.; Walther, P.; Alù, A.; Marini, A.; Cotrufo, M.; Queiroz, R.; Zhu, X.-Y.; Cox, J. D.; Dias, E. J. C.; Echarri, Á. R.; Iyikanat, F.; Herrmann, P.; Tornow, N.; Klimmer, S.; Wilhelm, J.; Soavi, G.; Sun, Z.; Wu, S.; Xiong, Y.; Matsyshyn, O.; Krishna Kumar, R.; Song, J. C. W.; Bucher, T.; Gorlach, A.; Tsesses, S.; Kaminer, I.; Schwab, J.; Mangold, F.; Giessen, H.; Sánchez, M. S.; Efetov, D. K.; Low, T.; Gómez-Santos, G.; Stauber, T.; Álvarez-Pérez, G.; Duan, J.; Martín-Moreno, L.; Paarmann, A.; Caldwell, J. D.; Nikitin, A. Y.; Alonso-González, P.; Mueller, N. S.; Volkov, V.; Jariwala, D.; Shegai, T.; Van De Groep, J.; Boltasseva, A.; Bondarev, I. V.; Shalaev, V. M.; Simon, J.; Fruhling, C.; Shen, G.; Novko, D.; Tan, S.; Wang, B.; Petek, H.; Mkhitaryan, V.; Yu, R.; Manjavacas, A.; Ortega, J. E.; Cheng, X.; Tian, R.; Mao, D.; Van Thourhout, D.; Gan, X.; Dai, Q.; Sternbach, A.; Zhou, Y.; Hafezi, M.; Litvinov, D.; Grzeszczyk, M.; Novoselov, K. S.; Koperski, M.; Papadopoulos, S.; Novotny, L.; Viti, L.; Vitiello, M. S.; Cottam, N. D.; Dewes, B. T.; Makarovsky, O.; Patanè, A.; Song, Y.; Cai, M.; Chen, J.; Naveh, D.; Jang, H.; Park, S.; Xia, F.; Jenke, P. K.; Bajo, J.; Braun, B.; Burch, K. S.; Zhao, L.; Xu, X. Roadmap for Photonics with 2D Materials. *ACS Photonics* **2025**, *12* (8), 3961−4095.

(3) Mak, K. F.; Lee, C.; Hone, J.; Shan, J.; Heinz, T. F. Atomically thin MoS$_2$: A new direct-gap semiconductor. *Phys. Rev. Lett.* **2010**, *105* (13), 136805.

(4) Long, M.; Wang, P.; Fang, H.; Hu, W. Progress, challenges, and opportunities for 2D material based photodetectors. *Adv. Funct. Mater.* **2019**, *29* (19), 1803807.

(5) Chernikov, A.; Berkelbach, T. C.; Hill, H. M.; Rigosi, A.; Li, Y.; Aslan, B.; Reichman, D. R.; Hybertsen, M. S.; Heinz, T. F. Exciton binding energy and nonhydrogenic Rydberg series in monolayer WS$_2$. *Phys. Rev. Lett.* **2014**, *113* (7), 076802.

(6) Wang, G.; Chernikov, A.; Glazov, M. M.; Heinz, T. F.; Marie, X.; Amand, T.; Urbaszek, B. Colloquium: Excitons in atomically thin transition metal dichalcogenides. *Rev. Mod. Phys.* **2018**, *90* (2), 021001.

(7) Ciccarino, C. J.; Christensen, T.; Sundararaman, R.; Narang, P. Dynamics and spin-valley locking effects in monolayer transition metal dichalcogenides. *Nano Lett.* **2018**, *18* (9), 5709−5715.

(8) Cao, T.; Wang, G.; Han, W.; Ye, H.; Zhu, C.; Shi, J.; Niu, Q.; Tan, P.; Wang, E.; Liu, B.; et al. Valley-selective circular dichroism of monolayer molybdenum disulphide. *Nat. Commun.* **2012**, *3* (1), 887.

(9) Zheng, D.; Zhang, S.; Deng, Q.; Kang, M.; Nordlander, P.; Xu, H. Manipulating coherent plasmon−exciton interaction in a single silver nanorod on monolayer WSe$_2$. *Nano Lett.* **2017**, *17* (6), 3809−3814.

(10) Wen, J.; Wang, H.; Wang, W.; Deng, Z.; Zhuang, C.; Zhang, Y.; Liu, F.; She, J.; Chen, J.; Chen, H.; et al. Room-Temperature Strong Light−Matter Interaction with Active Control in Single Plasmonic Nanorod Coupled with Two-Dimensional Atomic Crystals. *Nano Lett.* **2017**, *17* (8), 4689−4697.

(11) Luo, Y.; Zhao, J.; Fieramosca, A.; Guo, Q.; Kang, H.; Liu, X.; Liew, T. C. H.; Sanvitto, D.; An, Z.; Ghosh, S.; et al. Strong light-matter coupling in van der Waals materials. *Light: Sci. Appl.* **2024**, *13* (1), 203.

(12) Xiao, J.; Ye, Z.; Wang, Y.; Zhu, H.; Wang, Y.; Zhang, X. Nonlinear optical selection rule based on valley-exciton locking in monolayer WS$_2$. *Light: Sci. Appl.* **2015**, *4* (12), No. e366.

(13) Loh, L.; Ho, Y. W.; Xuan, F.; Del Águila, A. G.; Chen, Y.; Wong, S. Y.; Zhang, J.; Wang, Z.; Watanabe, K.; Taniguchi, T.; et al. Nb impurity-bound excitons as quantum emitters in monolayer WS$_2$. *Nat. Commun.* **2024**, *15* (1), 10035.

(14) Bauer, J. M.; Chen, L.; Wilhelm, P.; Watanabe, K.; Taniguchi, T.; Bange, S.; Lupton, J. M.; Lin, K.-Q. Excitonic resonances control the temporal dynamics of nonlinear optical wave mixing in monolayer semiconductors. *Nat. Photonics* **2022**, *16* (11), 777−783.

(15) Lepeshov, S.; Wang, M.; Krasnok, A.; Kotov, O.; Zhang, T.; Liu, H.; Jiang, T.; Korgel, B.; Terrones, M.; Zheng, Y.; Alú, A. Tunable Resonance Coupling in Single Si Nanoparticle−Monolayer WS $_2$ Structures. *ACS Appl. Mater. Interfaces* **2018**, *10* (19), 16690−16697.

(16) Krasnok, A.; Lepeshov, S.; Alú, A. Nanophotonics with 2D transition metal dichalcogenides. *Opt. Express* **2018**, *26* (12), 15972−15994.

(17) Huang, L.; Krasnok, A.; Alú, A.; Yu, Y.; Neshev, D.; Miroshnichenko, A. E. Enhanced light−matter interaction in two-dimensional transition metal dichalcogenides. *Rep. Prog. Phys.* **2022**, *85* (4), 046401.

(18) Maggiolini, E.; Polimeno, L.; Todisco, F.; Di Renzo, A.; Han, B.; De Giorgi, M.; Ardizzone, V.; Schneider, C.; Mastria, R.; Cannavale, A.; et al. Strongly enhanced light−matter coupling of monolayer WS$_2$ from a bound state in the continuum. *Nat. Mater.* **2023**, *22* (8), 964−969.

(19) Wu, S.; Buckley, S.; Schaibley, J. R.; Feng, L.; Yan, J.; Mandrus, D. G.; Hatami, F.; Yao, W.; Vučković, J.; Majumdar, A.; et al. Monolayer semiconductor nanocavity lasers with ultralow thresholds. *Nature* **2015**, *520* (7545), 69−72.

(20) Kleemann, M.-E.; Chikkaraddy, R.; Alexeev, E. M.; Kos, D.; Carnegie, C.; Deacon, W.; de Pury, A. C.; Große, C.; de Nijs, B.; Mertens, J.; et al. Strong-coupling of WSe$_2$ in ultra-compact plasmonic nanocavities at room temperature. *Nat. Commun.* **2017**, *8* (1), 1296.

(21) Kang, H.; Ma, J.; Li, J.; Zhang, X.; Liu, X. Exciton polaritons in emergent two-dimensional semiconductors. *ACS Nano* **2023**, *17* (24), 24449−24467.

(22) Ye, Y.; Wong, Z. J.; Lu, X.; Ni, X.; Zhu, H.; Chen, X.; Wang, Y.; Zhang, X. Monolayer excitonic laser. *Nat. Photonics* **2015**, *9* (11), 733−737.

(23) Wang, Z.; Dong, Z.; Zhu, H.; Jin, L.; Chiu, M.-H.; Li, L.-J.; Xu, Q.-H.; Eda, G.; Maier, S. A.; Wee, A. T. Selectively plasmon-enhanced second-harmonic generation from monolayer tungsten diselenide on flexible substrates. *ACS Nano* **2018**, *12* (2), 1859−1867.

(24) Tang, Y.; Zhang, Y.; Liu, Q.; Wei, K.; Cheng, X. A.; Shi, L.; Jiang, T. Interacting plexcitons for designed ultrafast optical nonlinearity in a monolayer semiconductor. *Light: Sci. Appl* **2022**, *11* (1), 94.

(25) Wang, Z.; Sebek, M.; Liang, X.; Elbanna, A.; Nemati, A.; Zhang, N.; Goh, C. H. K.; Jiang, M.; Pan, J.; Shen, Z.; et al. Greatly enhanced resonant exciton-trion conversion in electrically modulated atomically thin WS_2 at room temperature. *Adv. Mater.* **2023**, *35* (33), 2302248.

(26) Munkhbat, B.; Baranov, D. G.; Stührenberg, M.; Wersäll, M.; Bisht, A.; Shegai, T. Self-hybridized exciton-polaritons in multilayers of transition metal dichalcogenides for efficient light absorption. *ACS Photonics* **2019**, *6* (1), 139−147.

(27) Ling, H.; Li, R.; Davoyan, A. R. All van der Waals integrated nanophotonics with bulk transition metal dichalcogenides. *ACS Photonics* **2021**, *8* (3), 721−730.

(28) Zotev, P. G.; Wang, Y.; Andres-Penares, D.; Severs-Millard, T.; Randerson, S.; Hu, X.; Sortino, L.; Louca, C.; Brotons-Gisbert, M.; Huq, T.; et al. Van der Waals materials for applications in nanophotonics. *Laser Photonics Rev.* **2023**, *17* (8), 2200957.

(29) Ling, H.; Manna, A.; Shen, J.; Tung, H.-T.; Sharp, D.; Fröch, J.; Dai, S.; Majumdar, A.; Davoyan, A. R. Deeply subwavelength integrated excitonic van der Waals nanophotonics. *Optica* **2023**, *10* (10), 1345−1352.

(30) Zotev, P. G.; Bouteyre, P.; Wang, Y.; Randerson, S. A.; Hu, X.; Sortino, L.; Wang, Y.; Shegai, T.; Gong, S.-H.; Tittl, A.; Aharonovich, I.; Tartakovskii, A. I. Nanophotonics with multilayer van der Waals materials. *Nat. Photonics* **2025**, *19* (8), 788−802.

(31) Shen, F.; Zhang, Z.; Zhou, Y.; Ma, J.; Chen, K.; Chen, H.; Wang, S.; Xu, J.; Chen, Z. Transition metal dichalcogenide metaphotonic and self-coupled polaritonic platform grown by chemical vapor deposition. *Nat. Commun.* **2022**, *13* (1), 5597.

(32) Munkhbat, B.; Küçüköz, B.; Baranov, D. G.; Antosiewicz, T. J.; Shegai, T. O. Nanostructured transition metal dichalcogenide multilayers for advanced nanophotonics. *Laser Photonics Rev.* **2023**, *17* (1), 2200057.

(33) Verre, R.; Baranov, D. G.; Munkhbat, B.; Cuadra, J.; Käll, M.; Shegai, T. Transition metal dichalcogenide nanodisks as high-index dielectric Mie nanoresonators. *Nat. Nanotechnol.* **2019**, *14* (7), 679−683.

(34) Zotev, P. G.; Wang, Y.; Sortino, L.; Millard, T. S.; Mullin, N.; Conteduca, D.; Shagar, M.; Genco, A.; Hobbs, J. K.; Krauss, T. F.; et al. Transition Metal Dichalcogenide Dimer Nanoantennas for Tailored Light−Matter Interactions. *ACS Nano* **2022**, *16* (4), 6493−6505.

(35) Sung, J.; Shin, D.; Cho, H.; Lee, S. W.; Park, S.; Kim, Y. D.; Moon, J. S.; Kim, J.-H.; Gong, S.-H. Room-temperature continuous-wave indirect-bandgap transition lasing in an ultra-thin WS_2 disk. *Nat. Photonics* **2022**, *16* (11), 792−797.

(36) Zhang, H.; Abhiraman, B.; Zhang, Q.; Miao, J.; Jo, K.; Roccasecca, S.; Knight, M. W.; Davoyan, A. R.; Jariwala, D. Hybrid exciton-plasmon-polaritons in van der Waals semiconductor gratings. *Nat. Commun.* **2020**, *11* (1), 3552.

(37) Shin, D. -J.; Cho, H.; Sung, J.; Gong, S. -H. Direct observation of self-hybridized exciton-polaritons and their valley polarizations in a bare WS_2 layer. *Adv. Mater.* **2022**, *34* (50), 2207735.

(38) Popkova, A. A.; Antropov, I. M.; Tselikov, G. I.; Ermolaev, G. A.; Ozerov, I.; Kirtaev, R. V.; Novikov, S. M.; Evlyukhin, A. B.; Arsenin, A. V.; Bessonov, V. O.; et al. Nonlinear exciton-Mie coupling in transition metal dichalcogenide nanoresonators. *Laser Photonics Rev.* **2022**, *16* (6), 2100604.

(39) Randerson, S. A.; Zotev, P. G.; Hu, X.; Knight, A. J.; Wang, Y.; Nagarkar, S.; Hensman, D.; Wang, Y.; Tartakovskii, A. I. High Q hybrid Mie−plasmonic resonances in van der Waals nanoantennas on gold substrate. *ACS Nano* **2024**, *18* (25), 16208−16221.

(40) Ling, H.; Tang, Y.; Tian, X.; Shafirin, P.; Hossain, M.; Vabishchevich, P. P.; Harutyunyan, H.; Davoyan, A. R. Nonlinear van der Waals metasurfaces with resonantly enhanced light generation. *Nano Lett.* **2025**, *23* (25), 9229−9236.

(41) Weber, T.; Kühner, L.; Sortino, L.; Ben Mhenni, A.; Wilson, N. P.; Kühne, J.; Finley, J. J.; Maier, S. A.; Tittl, A. Intrinsic strong light-matter coupling with self-hybridized bound states in the continuum in van der Waals metasurfaces. *Nat. Mater.* **2023**, *22* (8), 970−976.

(42) Ding, Q.; Ashutosh, S.; Sortino, L.; Weber, T.; Kühner, L.; Maier, S. A.; Kruk, S.; Kivshar, Y.; Tittl, A.; Wang, W. Strong coupling and interfering resonances in isolated van der Waals nanoresonators. *arXiv*, **2025**.

(43) Wang, Y.; Louca, C.; Randerson, S.; Hu, X.; Zotev, P. G.; Chaundler, O. P.; Bouteyre, P.; Cheung, C. K.; Gorbachev, R.; Wang, Y. Exciton-polaritons in a monolayer semiconductor coupled to van der Waals dielectric nanoantennas on a metallic mirror. *arXiv*, **2025**.

(44) Nauman, M.; Yan, J.; de Ceglia, D.; Rahmani, M.; Zangeneh Kamali, K.; De Angelis, C.; Miroshnichenko, A. E.; Lu, Y.; Neshev, D. N. Tunable unidirectional nonlinear emission from transition-metal-dichalcogenide metasurfaces. *Nat. Commun.* **2021**, *12* (1), 5597.

(45) Xu, X.; Trovatello, C.; Mooshammer, F.; Shao, Y.; Zhang, S.; Yao, K.; Basov, D. N.; Cerullo, G.; Schuck, P. J. Towards compact phase-matched and waveguided nonlinear optics in atomically layered semiconductors. *Nat. Photonics* **2022**, *16* (10), 698−706.

(46) Panmai, M.; Xiang, J.; Zhou, L.; Li, S.; Lan, S. Revealing Mie Resonances with Enhanced and Suppressed Second-Order Nonlinear Optical Responses in a Hexagonal-Prism-Like MoS $_2$ Nanoparticle. *Laser Photonics Rev.* **2023**, *17* (11), 2300346.

(47) Zograf, G.; Polyakov, A. Y.; Bancerek, M.; Antosiewicz, T. J.; Küçüköz, B.; Shegai, T. O. Combining ultrahigh index with exceptional nonlinearity in resonant transition metal dichalcogenide nanodisks. *Nat. Photonics* **2024**, *18* (7), 751−757.

(48) Yu, T.; Panmai, M.; Li, S.; Liu, S.; Mao, Y.; Zhou, L.; Lan, S. Anisotropically enhanced second harmonic generation in a WS_2 nanoparticle driven by optical resonances. *ACS Appl. Nano Mater.* **2024**, *7* (1), 726−735.

(49) Biswas, R.; Prosad, A.; As, L. K.; Chatterjee, S.; Bag, U.; Konkada Manattayil, J.; Raghunathan, V. Leveraging strong electric field gradients at anapole resonances for enhanced second harmonic generation from molybdenum disulfide disks. *Adv. Mater.* **2025**, *37* (14), 2418257.

(50) Sortino, L.; Biechteler, J.; Lafeta, L.; Kühner, L.; Hartschuh, A.; Menezes, L. D. S.; Maier, S. A.; Tittl, A. Atomic-layer assembly of ultrathin optical cavities in van der Waals heterostructure metasurfaces. *Nat. Photonics* **2025**, *19* (8), 825−832.

(51) Zograf, G.; Küçüköz, B.; Polyakov, A. Y.; Yankovich, A. B.; Ranjan, A.; Bancerek, M.; Agrawal, A. V.; Olsson, E.; Wieczorek, W.; Antosiewicz, T. J.; et al. Ultrathin 3R-MoS_2 metasurfaces with atomically precise edges for efficient nonlinear nanophotonics. *Commun. Phys.* **2025**, *8* (1), 271.

(52) Li, C.; Liu, Z.; Chen, J.; Gao, Y.; Li, M.; Zhang, Q. Semiconductor nanowire plasmonic lasers. *Nanophotonics* **2019**, *8* (12), 2091−2110.

(53) Xiang, J.; Panmai, M.; Bai, S.; Ren, Y.; Li, G.-C.; Li, S.; Liu, J.; Li, J.; Zeng, M.; She, J.; et al. Crystalline silicon white light sources driven by optical resonances. *Nano Lett.* **2021**, *21* (6), 2397−2405.

(54) Zhou, L.; Panmai, M.; Li, S.; Mao, Y.; He, W.; Huang, H.; Lan, S. Lighting up Si nanoparticle arrays by exploiting the bound states in the continuum formed in a Si/Au hybrid nanostructure. *ACS Photonics* **2022**, *9* (9), 2991−2999.

(55) Hong, C.; Kim, H.; Tao, Y.; Lim, J. H.; Lee, J. Y.; Kim, J.-H. Ultrafast hot carrier extraction and diffusion at the MoS_2/Au van der Waals electrode interface. *Sci. Adv.* **2025**, *11* (1), No. eadr1534.

(56) Munkhbat, B.; Wróbel, P.; Antosiewicz, T. J.; Shegai, T. O. Optical constants of several multilayer transition metal dichalcogenides measured by spectroscopic ellipsometry in the 300−1700 nm range: High index, anisotropy, and hyperbolicity. *ACS Photonics* **2022**, *9* (7), 2398−2407.

(57) Shen, F.; Liu, D.; Chen, Z.; Zhu, J.; Jin, S.; Zhao, X.; Ma, Y.; Lei, D.; Xu, J. Manipulating the intrinsic light-matter interaction with high-Q resonances in an etch-free van der Waals metasurface. *Optica* **2025**, *12* (11), 1702−1711.

(58) Barreda, Á.; Vitale, F.; Minovich, A. E.; Ronning, C.; Staude, I. Applications of hybrid metal-dielectric nanostructures: State of the art. *Adv. Photonics Res.* **2022**, *3* (4), 2100286.

(59) Oliva, R.; Wozniak, T.; Faria, P. E., Jr.; Dybala, F.; Kopaczek, J.; Fabian, J.; Scharoch, P.; Kudrawiec, R. Strong substrate strain effects

in multilayered WS_2 revealed by high-pressure optical measurements. *ACS Appl. Mater. Interfaces* **2022**, *14* (17), 19857−19868.

(60) Johnson, P. B.; Christy, R.-W. Optical constants of the noble metals. *Phys. Rev. B* **1972**, *6* (12), 4370.